Fracture Resistance of Cu/Nb Metallic Nanolayered Composite

Sixie Huang and Caizhi Zhou\*

Department of Materials Science and Engineering, Missouri University of Science and

Technology, Rolla, MO 65409, USA

**Abstract** 

In this work, we perform molecular dynamics simulations to explore the crack propagation and

fracture behavior of Cu/Nb metallic nanolayered composites (MNCs). Our results are consistent

with previous experimental results, which illustrated that cracks in Cu and Nb layers may exhibit

different propagation paths and distances under the isostrain loading condition. The analysis

reveals that the interface can increase the fracture resistance of the Nb layer in Cu/Nb MNCs by

providing the dislocation sources to generate the plastic strain at the front of the crack. Increasing

the layer thickness can enhance the fracture resistance of both Cu and Nb layers, as the critical

stress for activating the dislocation motion decreases with the increment of the layer thickness. In

addition, grain boundaries (GBs) in polycrystalline Cu/Nb samples would decrease the fracture

resistance of Nb layer by promoting the crack propagate along the GBs, i.e. intergranular

fracture, while the effect of interface and layer thickness on the fracture resistance of MNCs will

1

not be altered by introducing the GBs in MNCs.

Key words: Nanolayer; Interface; Fracture behavior; Atomistic modeling; Crack propagation

\* Corresponding author.

E-mail address: zhouc@mst.edu

### 1. Introduction

Metallic nanolayered composites (MNCs) are nanostructured materials possessing impressive mechanical properties such as high strength, hardness and fatigue resistance, which can be fabricated by deposition or severe plastic deformation processes <sup>1-6</sup>. MNCs are composed of alternating layers of two or more metallic phases and the layer thickness of each phase are generally less than 100 nm. The interfaces between each layer play an critical role on the deformation of MNCs, as they can act as barriers, sink and sources of dislocations and vacancies <sup>7-9</sup>. Both experimental and computational studies have illustrated the remarkable thicknessdependent strength in MNCs that can be predicted by the confined layer slip (CLS) model <sup>10-13</sup>. Similar to nanocrystalline (NC) metallic materials, MNCs also exhibits an inverse relationship between the strength and elongation <sup>12, 14</sup>. To explore the fracture mechanisms in MNCs, Zhu at el. 15 examined the deformation zone ahead of the crack tip in the Cu/Ta MNCs and revealed a critical layer thickness, below which the fracture mode of the MNCs tends to be shearing failure. Zhang at el. 16 studied the fracture behavior of Cu/Nb and Cu/Zr. Their experiment results demonstrated that as the layer thickness of Cu layer decreased below 60 nm, the fracture mode in MNCs transited from brittle opening fracture to shear fracture. Based on their experiment results, they claimed that the transition of fracture modes is dominated by the constraint of the soft Cu layer on the brittle Nb or Zr layer. Hattar et al. <sup>17</sup> demonstrated four fracture steps (crack deviation, layer necking, microvoid formation and crack blunting) during the crack propagation in Cu/Nb by using the in-situ transmission electron microscopy testing. Radchenko et al. 18 found that the crack propagation under three-point bending in 63 nm Cu/Nb MNCs was inhibited by the interface shear. Atomistic simulations performed by Li et al. <sup>19</sup> also illustrated the weak

interface in Cu/Nb MNCs can hinder the crack propagation in Nb phase by interface shear and dislocation nucleation from interface.

Based on previous studies, we can see that in most MNCs, the plastic deformation ability is limited by the thickness of the each single layered phase. The interface in the MNCs can not only influence the strength of MNCs but also affect their ductility and the fracture behaviors. However, it is still unclear how the interface in MNCs affects the fracture mode of MNCs and how the crack interacts with the interface, especially for the cracks cutting through the layers. Atomistic simulations, such as molecular dynamics (MD) simulations, can shed light onto the failure mechanisms of NC materials by directly revealing the underlying atomic scale processes of the deformation and fracture. During the fracture, the crack propagation speed is comparable to speed of sound, and is well captured in the time frame of MD simulations. MD simulations have already been successfully used to explore the fracture behavior for NC metals, nanotwinned metals and gradient metals <sup>20-24</sup>. In this study, we perform MD simulations of the deformation in Cu/Nb MNCs with a preexisting crack to explore the crack propagation and fracture behavior of MNCs. Our simulation results show that the interface can increase the fracture resistance of the brittle Nb layer by providing the dislocation sources to generate the plastic strain at the front of the crack. The fracture resistance of both layers would be enhanced by increasing the layer thickness. Introducing grain boundaries (GBs) would decrease the fracture resistance of Nb layer, as the GBs act as the weakest location promoting the intergranular fracture.

#### 2. Materials

To study the effect of interface and the coupled effect of interface and grain boundaries on fracture behavior of MNCs, we adopt multiple types of samples in our model which include two-phase samples of single crystalline (SX) Cu/Nb, polycrystalline (PX) Cu/Nb, and single

phase samples of SX Cu, SX Nb, PX Cu, PX Nb. Figure 1 presents the examples of samples used in our calculations. Periodic boundary conditions have been applied along the thickness direction, which normally contains a large number of thin layers. As our study focuses on the mechanism of crack propagation within the nanolayers, this model may restrict a possibility of the shear localization that may take place at the final/catastrophic fracture stage. Fixed boundary conditions were set in other two directions under external loading. A pre-existing crack is created with the crack tip end at the center of each sample. To mimic the microstructure of Cu/Nb composites synthesized by the physical vapor deposition method (PVD) <sup>25</sup>, the crystallographic orientation for Cu layer is set as x-[11-2], y-[1-10], and z-[111], while the crystallographic orientation for Nb layer is set as x-[11-2], y-[111], and z-[1-10]. This configuration of Cu and Nb phases follows the Kurdjumov-Sachs (KS) orientation relationship <sup>26</sup>. The dimension of the simulation box was optimized to minimize the internal stresses. In the PX Cu/Nb samples, a modified Voronoi method <sup>27</sup> was used to create the nano grains with a hexagonal shape shown in Figure 1(b). The grain size for PX samples in this study set to be 10nm. We fixed one pair of Cu/Nb grains with the initial crystallographic orientation described above and rotated the neighboring grain pairs by 30°, 60° and 90° degree along the thickness direction shown in Figure 1 (b). In this way, stable large angle GBs can be created and the KS orientation relationship can still be maintained in each pairs of Cu/Nb grains, this method has also been used in previous MD simulations of polycrystalline Cu/Nb and Cu/Ag MNCs <sup>12, 28</sup>. Finally, to explore how the layer thickness affects the fracture behavior of MNCs, we vary the layer thickness of both SX Cu/Nb and PX Cu/Nb samples from 5 nm to 20 nm in our model.

# 3. Results and discussion

3.1 Single crystalline samples without grain boundaries

Figure 2 shows the atomistic structure for different SX samples at 15% engineering strain. The atoms in these figure were colored by the Green strain component  $\epsilon_{xx}$ . Figure 2 (a)-(c) present the samples for SX Cu, Cu layers in 5nm and 20 nm SX Cu/Nb samples, respectively. Crack tips in Cu for all three samples were blunted. The crack in SX Cu and Cu layer in 20nm SX Cu/Nb samples traveled almost the same distance at 15% strain, while the crack length in Cu layer of 5nm SX Cu/Nb sample is pronounced longer than previous two cases. Figure 2 (d)-(f) present the shape and propagation path of the crack in SX Nb, Nb layer of 5 nm and 20 nm SX Cu/Nb samples. It is obvious that the final lengths of the crack in Nb layer of SX Cu/Nb samples are shorter than that in the SX Nb sample. In addition, the larger the layer thickness of the SX Cu/Nb samples, the shorter the crack length is.

The specific crack tip propagation distances versus the applied strain for all samples are shown in Figure 3 (a). We can see that the crack propagation distances in SX Cu or Cu layers of SX Cu/Nb samples are all below 75 Å. While the crack propagation distances are always larger in SX Nb or Nb layer of SX Cu/Nb samples than that in Cu. Therefore, even if the initial preexisting crack position are the same in both Cu and Nb layers in Cu/Nb samples, crack propagation path and distance may be different for each phase in MNCs. This trend is consistent with experiment results <sup>17</sup> that the crack propagates/forms faster in Nb layer than in Cu layer as shown in Figure 4 (a) and (b).

Among the SX Nb sample and the Nb layer of SX Cu/Nb samples, the SX Nb sample has the largest crack propagation distance and fastest propagation rate shown in Figure 3 (a). It indicates that Cu/Nb interface can slow down the crack propagation rate and increase the fracture resistance ability in Nb layer. At 15% strain, the crack propagated distance has been decreases by 42% from 21 nm in SX Nb to 12 nm in Nb layer of 5nm SX Cu/Nb. Moreover, the improvement

of fracture resistance is more prominent in the thicker Nb layer. Compared to the SX Nb sample, the final propagation distance for Nb layer in 20nm SX Cu/Nb decrease from 21 to 6 nm. Thus, the thicker the sample, the better the crack resistance is in the Nb layer. This trend is also consistent with the results from previous experiment study by Kavarana et al. <sup>14</sup>, which demonstrated that that the ductility of MNCs increases with the bilayer thickness.

Figure 3 (b) shows the evolution of the stress intensity factor (SIF) versus the crack tip propagation distance. Similar to the trend shown in Figure 3 (a), SX Cu and Cu layer in Cu/Nb samples have larger SIF than those in the SX Nb and Nb layer in Cu/Nb. And SX Cu and Cu layer in 20 nm SX Cu/Nb carry similar values of SIFs over the same crack tip propagation range and both of them are larger than that for Cu layer in 5nm SX Cu/Nb sample. In addition, the SIFs for Nb layer in Cu/Nb samples are larger than that for the SX Nb. And also the larger the layer thickness, the higher SIFs of each phase in Cu/Nb samples.

Since no GBs exist in all SX samples, Green strain shown in Figure 2 should totally result from the dislocation activities. The Green strains in Nb layers of SX Cu/Nb samples are more uniform than that in the SX Nb sample. That indicates more slip systems in the Nb layer of SX Cu/Nb samples were activated which led to a more homogeneous plastic deformation, while the activated dislocation activities were more focused on one or two slip systems in SX Nb sample. Figure 3 (c) compares the total green strains induced by dislocation activities per volume for SX samples. It is clear that at the same applied strain, the Green strains induced by dislocation activities are higher in SX Cu and Cu layer in Cu/Nb than those in Nb phase or layers. The evolution of the Green strain in each case is consistent well with the crack propagation distance shown in Figure 3(a) and SIFs in Figure 3(b). The phase with higher SIF and shorter crack propagation distance normally contains larger Green strain. In metallic materials, there are

two ways to release the excess elastic energy stored within the materials: i) creating new surfaces by opening cracks, ii) changing the shape of the material via plastic deformation. In the SX samples, the plastic deformation was mainly induced by the dislocation activities. Thus, larger Green strain under the same applied strain indicates more plastic deformation induced by dislocation activates that suppressed the crack propagation to create new surfaces. In the Cu/Nb samples, the interface provides dislocation sources for nucleating interfacial dislocations into each phase as shown in Figure 4 (c) and (d). Thus, the Nb layers in Cu/Nb samples own more Green strain than the SX Nb sample. In addition, thicker Cu/Nb samples carry larger Green stains in both Cu and Nb layers. That is because the confined layer slip (CLS) is the main dislocation activity in the SX Cu/Nb samples as shown in Figure 4 (d). The critical stress for activating confined layer slips is inversely proportional to the layer thickness as the following <sup>11</sup>:

$$\tau_{CLS} = \frac{\mu b \sin \varphi}{8\pi h} \left(\frac{4-v}{1-v}\right) \ln \frac{\alpha h}{b \sin \varphi} \tag{3}$$

where h is the layer thickness,  $\mu$  the shear modulus,  $\nu$  the Poisson's ratio,  $\varphi$  the angle between slip plane and the layer interface, b the Burgers vector of dislocation, and  $\alpha$  is a coefficient representing the extent of dislocation core. Therefore, the larger the layer thickness, the smaller the critical stress is to activate dislocation motion within the layer. The dislocation induced plasticity would increase with the layer thickness, and therefore increase the Green strain and suppress the crack propagation. In SX samples, dislocations can only come from the crack tip due to the high stress concentration, and the number of dislocation sources is limited. In contrast, the available dislocation sources are plenteous in Cu/Nb sample due to the high density of interfacial dislocation networks  $^{9,29}$ . That is why the Green strain in Cu layer in 20 nm Cu/Nb sample is even larger than that in the SX Cu sample.

## 3.2 Polycrystalline samples with grain boundaries

Figure 5 shows the atomistic structure for different PX samples at 12 % engineering strain. Figure 5 (a)-(c) present the samples for PX Cu, Cu layers in 5nm and 20 nm PX Cu/Nb samples, respectively. For PX Cu, the crack propagated within the initial grain firstly. After the tip approach the GBs, the propagation stopped and the crack was blunted at GBs as shown in Figure 5 (a). For the Cu layer in 5 nm PX Cu/Nb sample, after the preexisting crack approached the closest GBs, it continued growing along other GBs. That induced the intergranular fracture in the thin Cu layer. However, when the layer thickness of Cu layer increased to 20 nm, the intergranular fracture disappeared and crack also was blunted at GBs as shown in Figure 5 (c). According to the CLS model, the critical stress for dislocation slip within each thin layer in 20nm samples is much lower than that for 5nm samples. Thus, more dislocations can slip at the front of the crack, especially those nucleating from the GBs, to release the elastic energy and blunt the crack tip in the 20nm sample rather than open new surfaces at the front of the crack along the GBs.

Figure 5 (d)-(f) present the shape and propagation path of the crack in PX Nb, Nb layer in 5 nm and 20 nm PX Cu/Nb samples, respectively. Although cracks in all three samples propagated along the GBs, differences still exist between the PX Nb and Nb layer in the PX Cu/Nb samples. In PX Nb, multiple cracks nucleated at the GBs in the front of the preexisting crack. Those newly formed cracks grow along the GBs. Once they coalesced with the preexisting crack, a long crack formed across multiple GBs. While the crack in Cu/Nb grow much slower and little or less new cracks nucleated at the front of the preexisting crack.

Figure 6 (a) plot the crack propagation distance versus the engineering stain for all PX samples. From the plot, we can see the crack propagation process for PX Cu sample is nearly the same as that in Cu layer of 20 nm PX Cu/Nb sample. Since there was no crack blunting, the

crack propagation distance in Cu layer of 5 nm PX Cu/Nb sample is striking larger than the PX Cu after 6% strain. This phenomenon may be caused by the suppression of dislocation nucleation at interface when the layer thickness is small. The interfaces may improve the fracture resistance of in the Cu layer, but the opposing effect of the GBs make the overall crack resistance deteriorate. As the layer thickness increases from 5nm to 20 nm, the fracture resistance ability of Cu layer in Cu/Nb MNCs may recover to the same level as single phase PX Cu sample. Therefore, the interfaces can improve the fracture resistance. Figure 6 (a) also indicate that the trend of crack propagation distance for PX Nb and Nb layer in PX Cu/Nb samples is similar to that in SX samples: i) introducing the Cu/Nb interface improved the fracture resistance of the Nb layer, ii) the thicker the samples, the better crack resistance is. As shown in Figure 5 (g), dislocations nucleate from the interface at the front of crack, due to the high stress concentration at the front of the crack. Therefore, in the PX Cu/Nb samples, the interface also can provide dislocation sources for nucleating interfacial dislocations into each phase. Figure 6 (b) shows the fracture toughness curves for all PX samples. We can see that, at the same crack tip propagation distance, the value of SIFs in the 20 nm Cu layer and single phase PX Cu are the same, both of which are larger than the SIF in 5 nm Cu layer. For Nb, the SIF of 5 nm Nb layer is the lowest one among the three cases. The SIF curves for 20 nm Nb and PX Nb overlap each other for the first 50 Å. After the crack propagated 50 Å, the SIF curve of 20 nm Nb deviated from the PX Nb curve. That means the Cu/Nb interface suppressed the crack propagation and increased the SIF in the 20 nm Cu/Nb.

Figure 6 (c) compares the total Green strain induced in PX samples. The Green strain induced by grain boundaries atoms were not considered on this plot, as the shape, size of grains and the GBs types are exactly the same for all PX samples. It is clear that the Green strain in the

PX Cu samples is always the highest one among all cases, followed by the Cu layer in 20 nm Cu/Nb sample. While the single phase PX Nb displays lowest Green strain for the full range of applied strain. This trend is consistent with the crack propagation distance plot in Figure 6 (a). Since the excess stored elastic energy can either be released by the crack propagation or the dislocation slip, larger Green strains induced by the dislocation slip can suppress the crack propagation and increase the SIF. Thus, the Green strains in Nb layers bonded by the Cu/Nb interfaces are higher than that in the single phase PX Nb, and increasing the layer thickness can facilitate the dislocation activities to generate more Green strains.

### 4. Conclusion

In this work, we studied the fracture resistance of single crystalline and polycrystalline Cu/Nb MNCs by using MD simulations. Our simulation results are consistent with previous experiment results, which revealed that cracks in Cu and Nb layers may exhibit different propagation paths and distances under the isostrain loading condition. Nb layer in Cu/Nb samples exhibited better fracture resistance compared with the single phase Nb samples, as the interface can provide abundant dislocation sources for plastic deformation at the crack tip that can suppress the crack propagation and increase the fracture resistance in MNCs. Compared with the single crystalline Cu samples, the Cu/Nb interface would deteriorate the fracture resistance of Cu layer when the layer thickness of Cu layer is below 20 nm. While with the layer thickness increases to 20 nm, the Cu layers in the MNCs possess a similar fracture resistance as that in the single phase Cu samples, as the CRSS to drive the dislocation motion decrease with the increment of the layer thickness. GBs in polycrystalline Cu/Nb samples would decrease the fracture resistance of both Cu and Nb layer by promoting the intergranular fracture, so the effect of interface may be not be

as prominent as that in SX Cu/Nb samples when the layer thickness is small, while the effect of layer thickness on the fracture resistance will not be altered by the GBs. Our findings in this work can provide fundamental understanding of the fracture behavior of MNCs and have implications for the design of nanostructured materials with better fracture resistance.

### Methods

We perform the MD simulation by using Large-scale Atomic/Molecular Massively Parallel simulator (LAMMPS) codes <sup>30</sup>. Interatomic potential based on Embedded Atom Method (EAM) was used to describe the force between each atom. Potential developed by Mishin et al, Ackland et al and Zhang et al were used to describe the interatomic force for Cu-Cu, Nb-Nb and Cu-Nb respectively <sup>2, 31, 32</sup>. These potential have been used widely in the last decade for many studies and provided a lot of insight for understanding the deformation mechanism <sup>33-36</sup>.

Before experiencing loading, the samples were relaxed by the conjugate gradient method firstly, then equilibrated at 300K for about 40 ps by the Nose/Hoover isobaric-isothermal ensemble (NPT)  $^{27}$  and the pressure in Z direction was kept zero  $^{37,38}$ . After relaxation, we load the sample by increasing the stress intensity factor of  $0.015 \text{ MPa}\sqrt{m}$  per step based on the fracture mechanics solution for mode-I fracture  $^{21}$ . During the each loading step, the boundary atoms within 1 nm from the edge in X and Y directions were fixed while other mobile atoms were allowed to relax for 1 ps. The crack tip was recorded to extract the crack length at a specific applied strain. Common neighbor analysis method  $^{32}$  and Green strain tensor  $^{39}$  were calculated to characterize the microstructure evolution. Dislocation structures were generated by the dislocation extraction algorithm (DXA)  $^{40}$ . Finally, the atomistic structures were visualized by the software OVITO  $^{41}$ .

To determine the Green strain,  $E_{ij}$ , for each atom, we firstly calculated the local deformation gradient tensor F for each atom based on the derivative of the relative displacements of the atom's neighbors

$$\mathbf{F}_{iI} = \frac{\partial x}{\partial X} \tag{1}$$

where  $\mathbf{X} = [X_1, X_2, X_3]$  is the original distance vector for atoms to their references before deformation, and  $\mathbf{x} = [x_1, x_2, x_3]$  is the new distance vector during deformation. The neighboring atoms should locate within a cutoff radius for 3.5 Angstrom, which can include at least three non-coplanar neighbors for the targeted atom <sup>42</sup>. Then the Green strain  $E_{ij}$  is calculated by:

$$\boldsymbol{E}_{ij} = \frac{1}{2} (\boldsymbol{F}_{iI} \boldsymbol{F}_{ij} - \delta_{IJ}) \tag{2}$$

where  $\delta_{II}$  is the identity tensor.

## Acknowledgments

This work was supported by the grants from NSF CAREER Award (CMMI-1652662). The supercomputer time allocation for completing the atomistic simulations was provided by the Extreme Science and Engineering Discovery Environment (XSEDE), award number DMR170093.

#### References

- 1. T. Höchbauer, A. Misra, K. Hattar and R. Hoagland: Influence of interfaces on the storage of ion-implanted He in multilayered metallic composites *Journal of applied physics.* **98**(12), 123516 (2005).
- 2. A. Misra, J. Hirth, R. Hoagland, J. Embury and H. Kung: Dislocation mechanisms and symmetric slip in rolled nano-scale metallic multilayers *Acta materialia*. **52**(8), 2387 (2004).
- 3. Y.-C. Wang, A. Misra and R. Hoagland: Fatigue properties of nanoscale Cu/Nb multilayers *Scripta materialia*. **54**(9), 1593 (2006).
- 4. A. Misra, M. Demkowicz, X. Zhang and R. Hoagland: The radiation damage tolerance of ultra-high strength nanolayered composites *Jom.* **59**(9), 62 (2007).

- 5. S. Shao and S.N. Medyanik: Interaction of dislocations with incoherent interfaces in nanoscale FCC BCC metallic bi-layers *Modelling and Simulation in Materials Science and Engineering.* **18**(5), 055010 (2010).
- 6. S. Shao, H.M. Zbib, I. Mastorakos and D.F. Bahr: Effect of Interfaces in the Work Hardening of Nanoscale Multilayer Metallic Composites During Nanoindentation: A Molecular Dynamics Investigation *Journal of Engineering Materials and Technology*. **135**(2), 021001 (2013).
- 7. R.G. Hoagland, R.J. Kurtz and C. Henager Jr: Slip resistance of interfaces and the strength of metallic multilayer composites *Scripta materialia*. **50**(6), 775 (2004).
- 8. I. Mastorakos, N. Abdolrahim and H. Zbib: Deformation mechanisms in composite nanolayered metallic and nanowire structures *International Journal of Mechanical Sciences*. **52**(2), 295 (2010).
- 9. S. Shao, J. Wang, I.J. Beyerlein and A. Misra: Glide dislocation nucleation from dislocation nodes at semi-coherent {111} Cu-Ni interfaces *Acta Materialia*. **98**, 206 (2015).
- 10. A. Misra, J. Hirth and H. Kung: Single-dislocation-based strengthening mechanisms in nanoscale metallic multilayers *Philosophical Magazine A.* **82**(16), 2935 (2002).
- 11. A. Misra, J. Hirth and R. Hoagland: Length-scale-dependent deformation mechanisms in incoherent metallic multilayered composites *Acta materialia*. **53**(18), 4817 (2005).
- 12. S. Huang, I.J. Beyerlein and C. Zhou: Nanograin size effects on the strength of biphase nanolayered composites *Scientific Reports*. 7(1), 11251 (2017).
- 13. S. Huang, J. Wang and C. Zhou: Effect of plastic incompatibility on the strain hardening behavior of Al–TiN nanolayered composites *Materials Science and Engineering: A.* **636**, 430 (2015).
- 14. F. Kavarana, K. Ravichandran and S. Sahay: Nanoscale steel-brass multilayer laminates made by cold rolling: microstructure and tensile properties *Scripta materialia*. **42**(10), 947 (2000).
- 15. X.F. Zhu, Y.P. Li, G.P. Zhang, J. Tan and Y. Liu: Understanding nanoscale damage at a crack tip of multilayered metallic composites *Applied Physics Letters*. **92**(16), 1 (2008).
- 16. J.Y. Zhang, X. Zhang, R.H. Wang, S.Y. Lei, P. Zhang, J.J. Niu, G. Liu, G.J. Zhang and J. Sun: Length-scale-dependent deformation and fracture behavior of Cu/ (X = Nb, Zr) multilayers: The constraining effects of the ductile phase on the brittle phase *Acta Materialia*. **59**(19), 7368 (2011).
- 17. K. Hattar, A. Misra, M.R.F. Dosanjh, P. Dickerson, I.M. Robertson and R.G. Hoagland: Direct Observation of Crack Propagation in Copper–Niobium Multilayers *Journal of Engineering Materials & Technology.* **134**(2), 021014 (2012).
- 18. I. Radchenko, H.P. Anwarali, S.K. Tippabhotla and A.S. Budiman: Effects of Interface Shear Strength during Failure of Semicoherent Metal–Metal Nanolaminates: An Example of Accumulative Roll-bonded Cu/Nb *Acta Materialia*. (2018).
- 19. Y. Li, Q. Zhou, S. Zhang, P. Huang, K. Xu, F. Wang and T. Lu: On the role of weak interface in crack blunting process in nanoscale layered composites *Applied Surface Science*. **433**, (2018).
- 20. S. Huang, J. Wang, N. Li, J. Zhang and C. Zhou: Atomistic simulations of plasticity in heterogeneous nanocrystalline Ni lamella *Computational Materials Science*. **141**, 229 (2018).

- 21. A. Latapie and D. Farkas: Molecular dynamics investigation of the fracture behavior of nanocrystalline α-Fe *Physical Review B.* **69**(13), 460 (2004).
- 22. H. Zhou, S. Qu and W. Yang: Toughening by nano-scaled twin boundaries in nanocrystals *Modelling and Simulation in Materials Science and Engineering.* **18**(6), 065002 (2010).
- 23. Z. Zeng, X. Li, L. Lu and T. Zhu: Fracture in a thin film of nanotwinned copper *Acta Materialia*. **98**, 313 (2015).
- 24. S. Huang, J. Wang and C. Zhou: Deformation of Heterogeneous Nanocrystalline Lamella with a Preexisting Crack *JOM*. **70**(1), 60 (2018).
- 25. A. Misra and H. Krug: Deformation behavior of nanostructured metallic multilayers *Advanced Engineering Materials*. **3**(4), 217 (2001).
- 26. R.G. Hoagland, R.J. Kurtz and C.H. Henager: Slip resistance of interfaces and the strength of metallic multilayer composites *Scripta Materialia*. **50**(6), 775 (2004).
- 27. J. Schiøtz, T. Vegge, F.D. Di Tolla and K.W. Jacobsen: Atomic-scale simulations of the mechanical deformation of nanocrystalline metals *Physical Review B.* **60**(17), 11971 (1999).
- 28. Y. Zhu, Z. Li and M. Huang: The size effect and plastic deformation mechanism transition in the nanolayered polycrystalline metallic multilayers *Journal of Applied Physics.* **115**(23), 233508 (2014).
- 29. S. Shao, J. Wang, A. Misra and R.G. Hoagland: Spiral Patterns of Dislocations at Nodes in (111) Semi-coherent FCC Interfaces *Scientific Reports*. **3**, 2448 (2013).
- 30. S. Plimpton: Fast Parallel Algorithms for Short-Range Molecular Dynamics *Journal of Computational Physics.* **117**(1), 1 (1995).
- 31. Z. Liang, M. Enrique, C. Alfredo, L. Xiang-Yang and J.D. Michael: Liquid-phase thermodynamics and structures in the Cu–Nb binary system *Modelling and Simulation in Materials Science and Engineering.* **21**(2), 025005 (2013).
- 32. J.D. Honeycutt and H.C. Andersen: Molecular dynamics study of melting and freezing of small Lennard-Jones clusters *The Journal of Physical Chemistry.* **91**(19), 4950 (1987).
- 33. I.N. Mastorakos, A. Bellou, D.F. Bahr and H.M. Zbib: Size-dependent strength in nanolaminate metallic systems *Journal of Materials Research.* **26**(10), 1179 (2011).
- 34. N. Abdolrahim, H.M. Zbib and D.F. Bahr: Multiscale modeling and simulation of deformation in nanoscale metallic multilayer systems *International journal of plasticity*. **52**, 33 (2014).
- 35. E. Martínez, A. Caro and I.J. Beyerlein: Atomistic modeling of defect-induced plasticity in CuNb nanocomposites *Physical review b.* **90**(5), 054103 (2014).
- 36. J. Zhou, R. Averback and P. Bellon: Stability and amorphization of Cu–Nb interfaces during severe plastic deformation: Molecular dynamics simulations of simple shear *Acta Materialia*. **73**, 116 (2014).
- 37. W.G. Hoover: Constant-pressure equations of motion *Physical Review A.* **34**(3), 2499 (1986).
- 38. S. Nosé: A unified formulation of the constant temperature molecular dynamics methods *Journal of Chemical Physics.* **81**(1), 511 (1984).
- 39. J.A. Zimmerman, D.J. Bammann and H. Gao: Deformation gradients for continuum mechanical analysis of atomistic simulations *International Journal of Solids and Structures.* **46**(2), 238 (2009).

- 40. A. Stukowski, V.V. Bulatov and A. Arsenlis: Automated identification and indexing of dislocations in crystal interfaces *Modelling and Simulation in Materials Science and Engineering.* **20**(8), 085007 (2012).
- 41. A. Stukowski: Visualization and analysis of atomistic simulation data with OVITO—the Open Visualization Tool *Modelling and Simulation in Materials Science and Engineering*. **18**(1), 015012 (2009).
- 42. Y. Zhang, G.J. Tucker and J.R. Trelewicz: Stress-assisted grain growth in nanocrystalline metals: Grain boundary mediated mechanisms and stabilization through alloying *Acta Materialia*. **131**, 39 (2017).

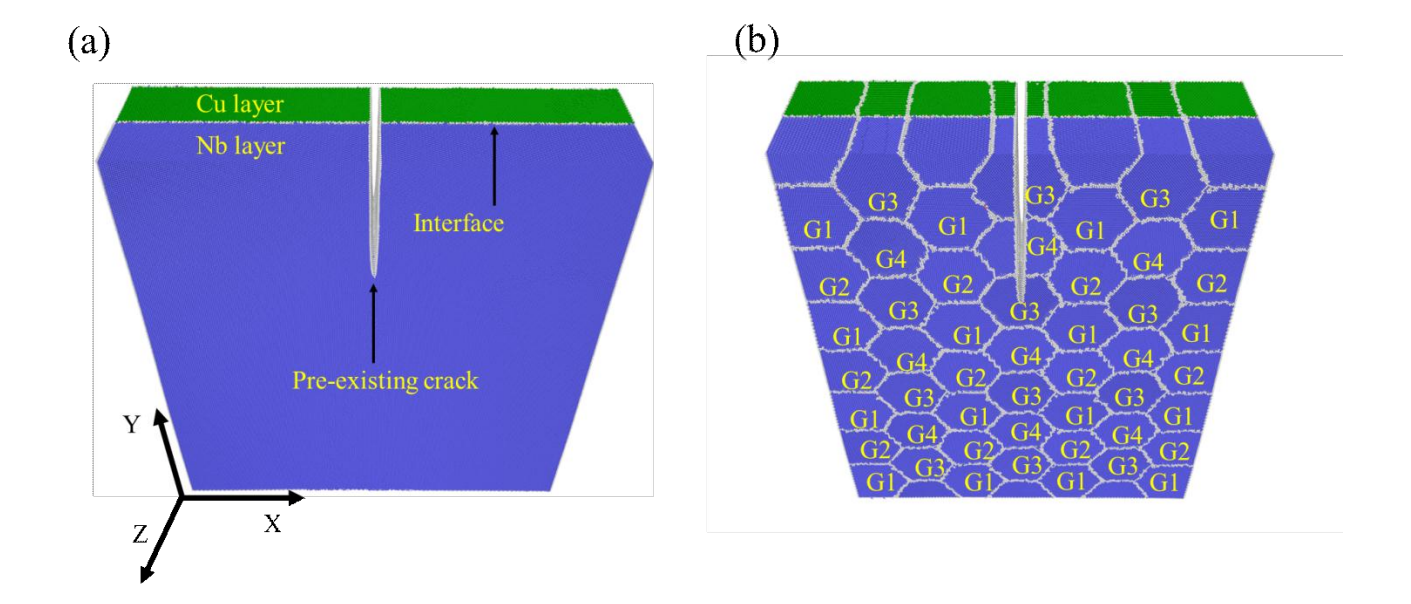


Figure 1. Initial configuration of Cu/Nb samples with a preexisting crack: (a) single crystalline (SX) Cu/Nb sample, (b) polycrystalline (PX) Cu/Nb samples. (Atoms colored by the CAN method. Atoms with green, blue and white represent the FCC, BCC and unknown atoms, respectively. The unknown atoms general represent the atoms locate at grain boundaries and interface.) The crystallographic orientation for Cu layer is set as x-[11 $\overline{2}$ ], y-[1 $\overline{1}$ 0], and z-[111], while the crystallographic orientation for Nb layer is set as x-[11 $\overline{2}$ ], y-[111], and z-[1 $\overline{1}$ 0]. G1 have the same crystallographic orientation in (a), G2, G3,G4 were rotated by 30°, 60° and 90° degree along the Z-axis.

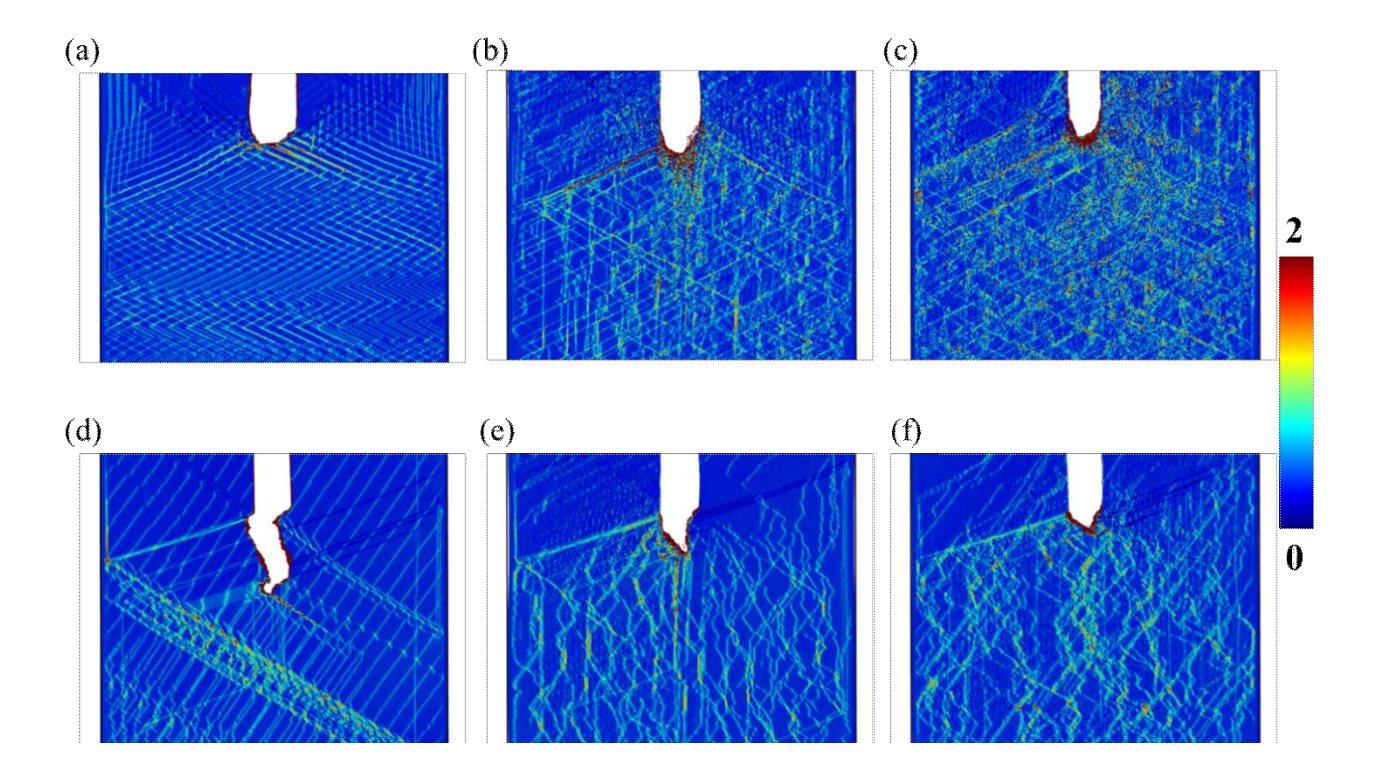


Figure 2. Atomistic structures for different samples at 15% strain, atoms colored by the green strain tensor component,  $\varepsilon_{xx}$ . (a) SX Cu, (b) Cu layer in 5 nm SX Cu/Nb, (c) Cu layer in 20 nm SX Cu/Nb, (d) SX Nb, (e) Nb layer in 5 nm SX Cu/Nb, (f) Nb layer in 20 nm SX Cu/Nb.

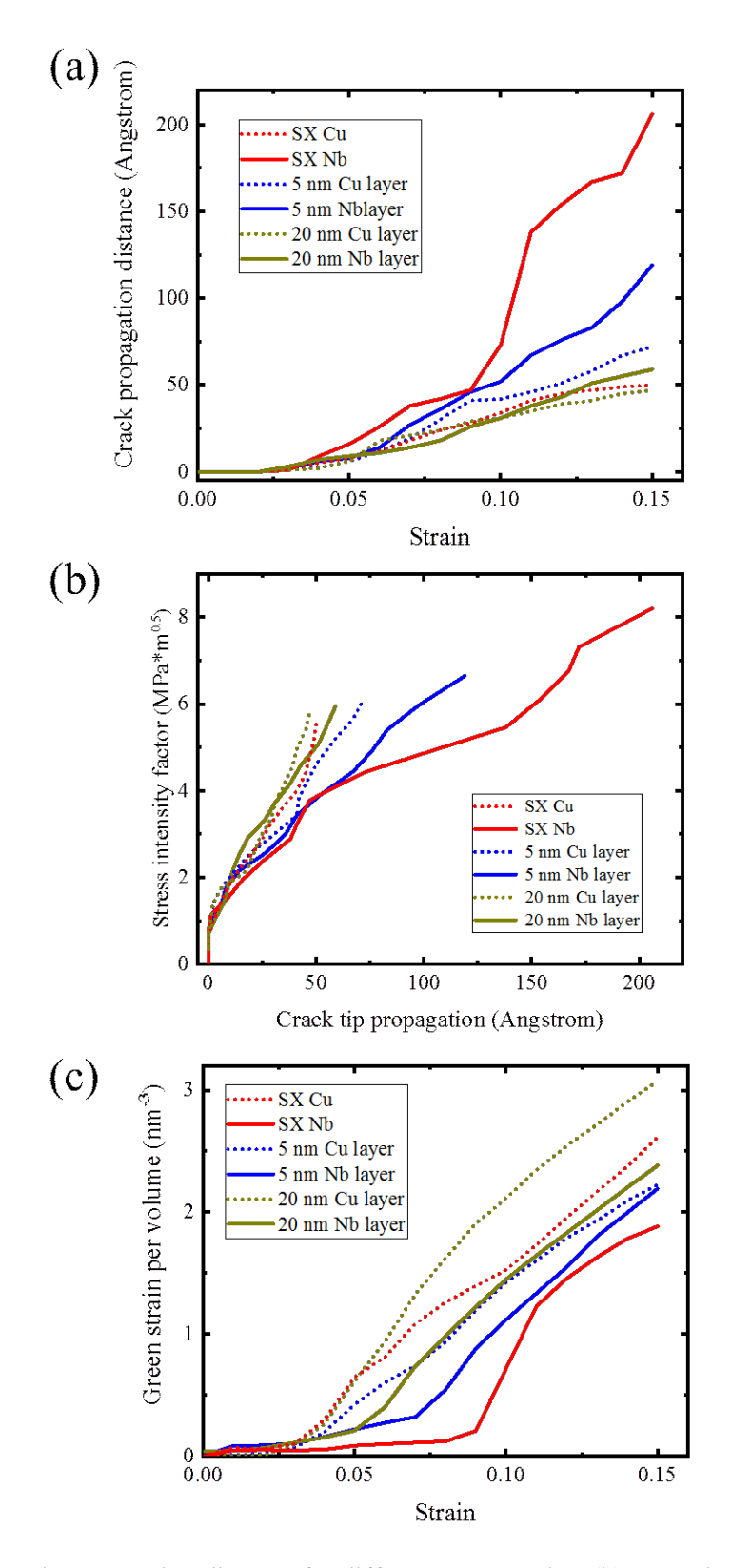


Figure 3. (a) Plot of crack propagation distance for different SX samples. (b) Stress intensity factor curves for different SX sample. (c) Green strain per volume for different SX samples.

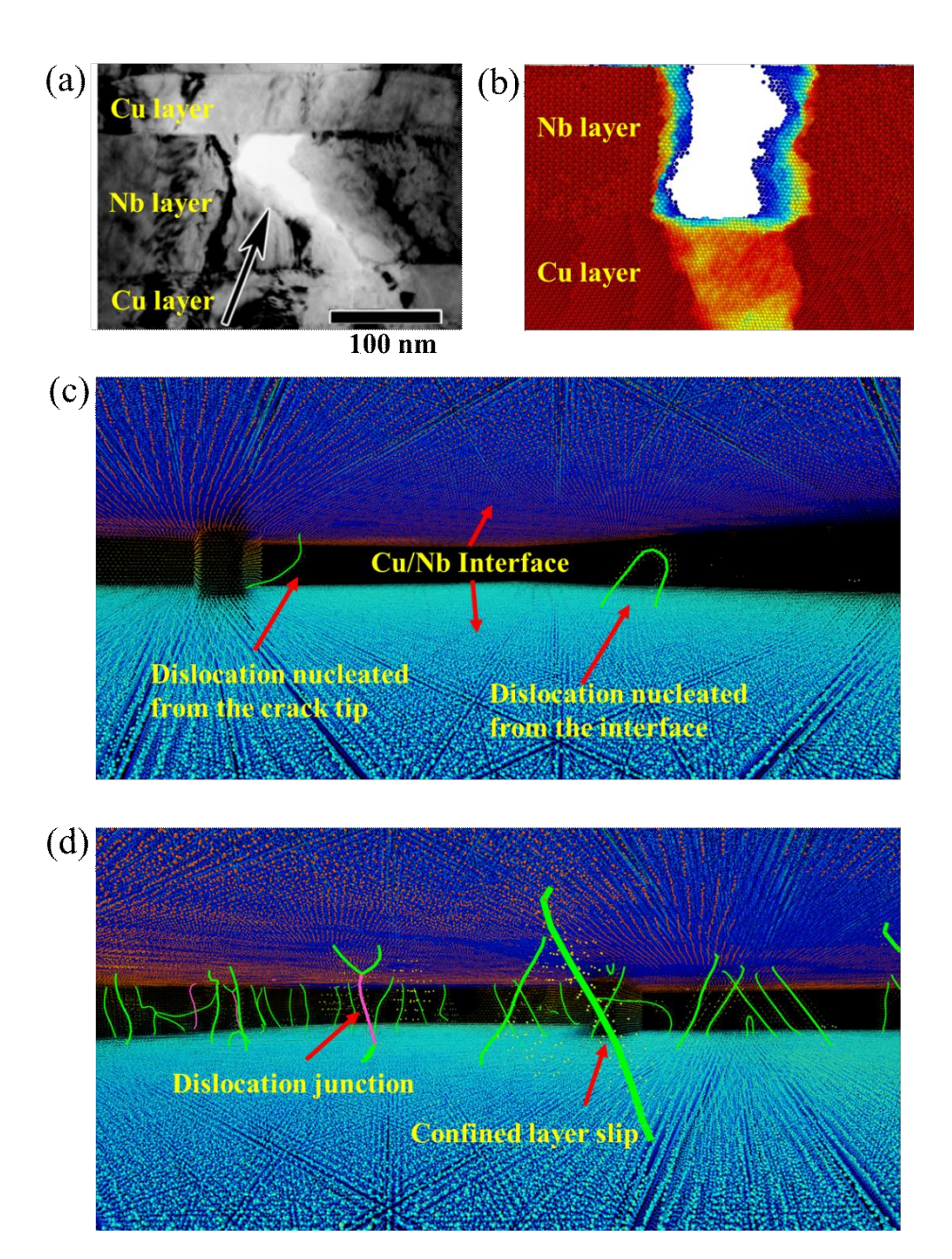


Figure 4. (a) One crack in Cu/Nb MNCs from the experimental work <sup>18</sup>. (b) One crack in SX Cu/Nb samples in this study (The fractured layer is Nb layer and atoms were colored by their Y coordinate. Note: the crack growth direction is perpendicular to the paper in both experimental and simulation tests). (c) Dislocation nucleating from the interface and crack tip (Atoms with BCC type were set invisible. Atoms were colored by their Z coordinate. Dislocations with green colors is for 1/2 <111> in {110} slip system.). (d) Confined layer slip of dislocations. (Dislocations with purple colors represent the dislocation junction.)

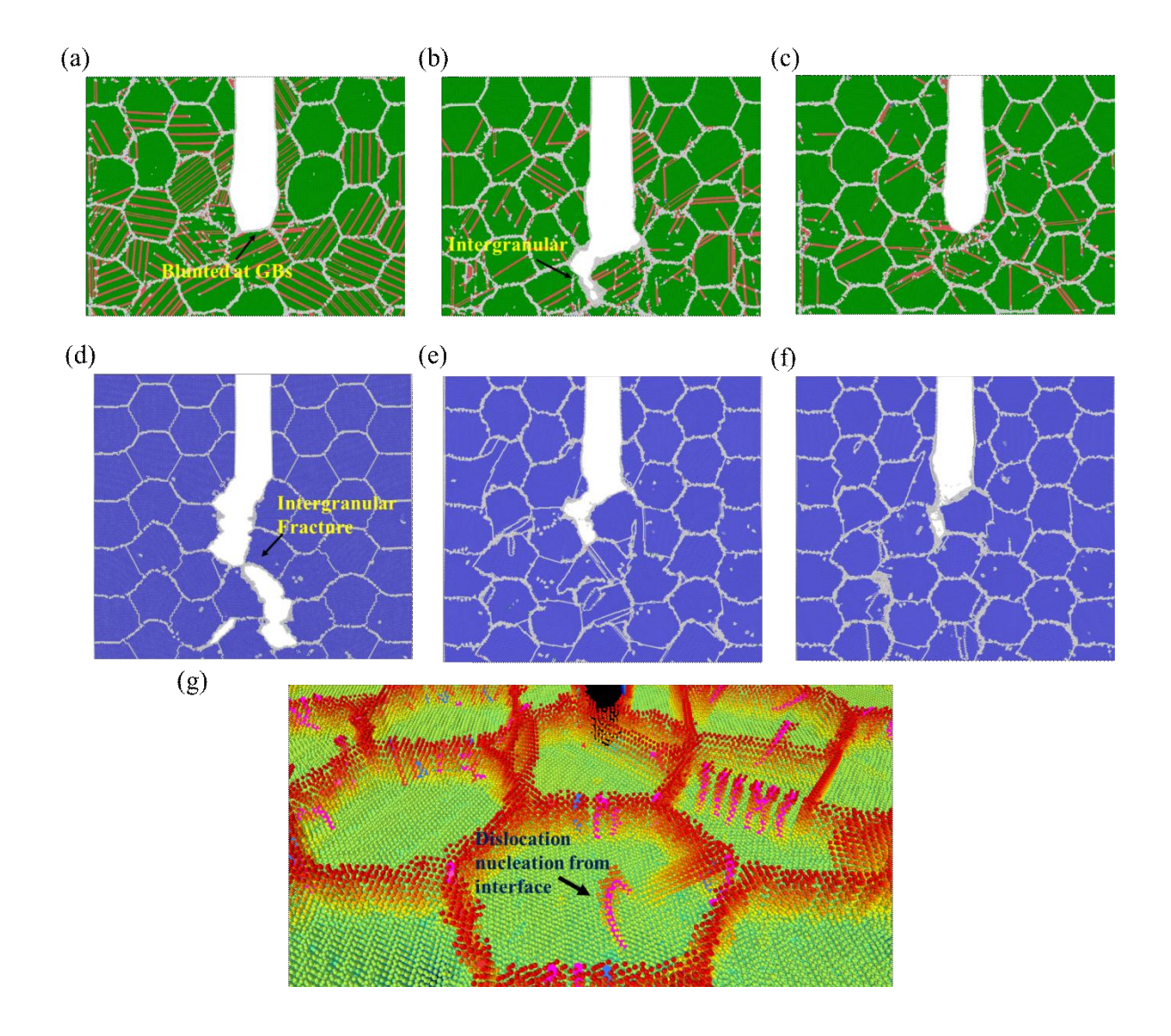


Figure 5. Atomistic structures for different PX sample at 12% strain: (a) PX Cu, (b) Cu layer in 5 nm PX Cu/Nb, (c) Cu layer in 20 nm PX Cu/Nb, (d) PX Nb, (e) Nb layer in 5 nm PX Cu/Nb, (f) Nb layer in PX 20 nm Cu/Nb, and (g) one example of the dislocation nucleating from the interface at the front of the crack within the Nb layer in 20 nm PX Cu/Nb sample. Atoms belong BCC and FCC atom are set invisible, and Atoms were colored by their Z coordinate. The purple line represents the dislocation line which belong to 1/2 <111> in {110} slip system.

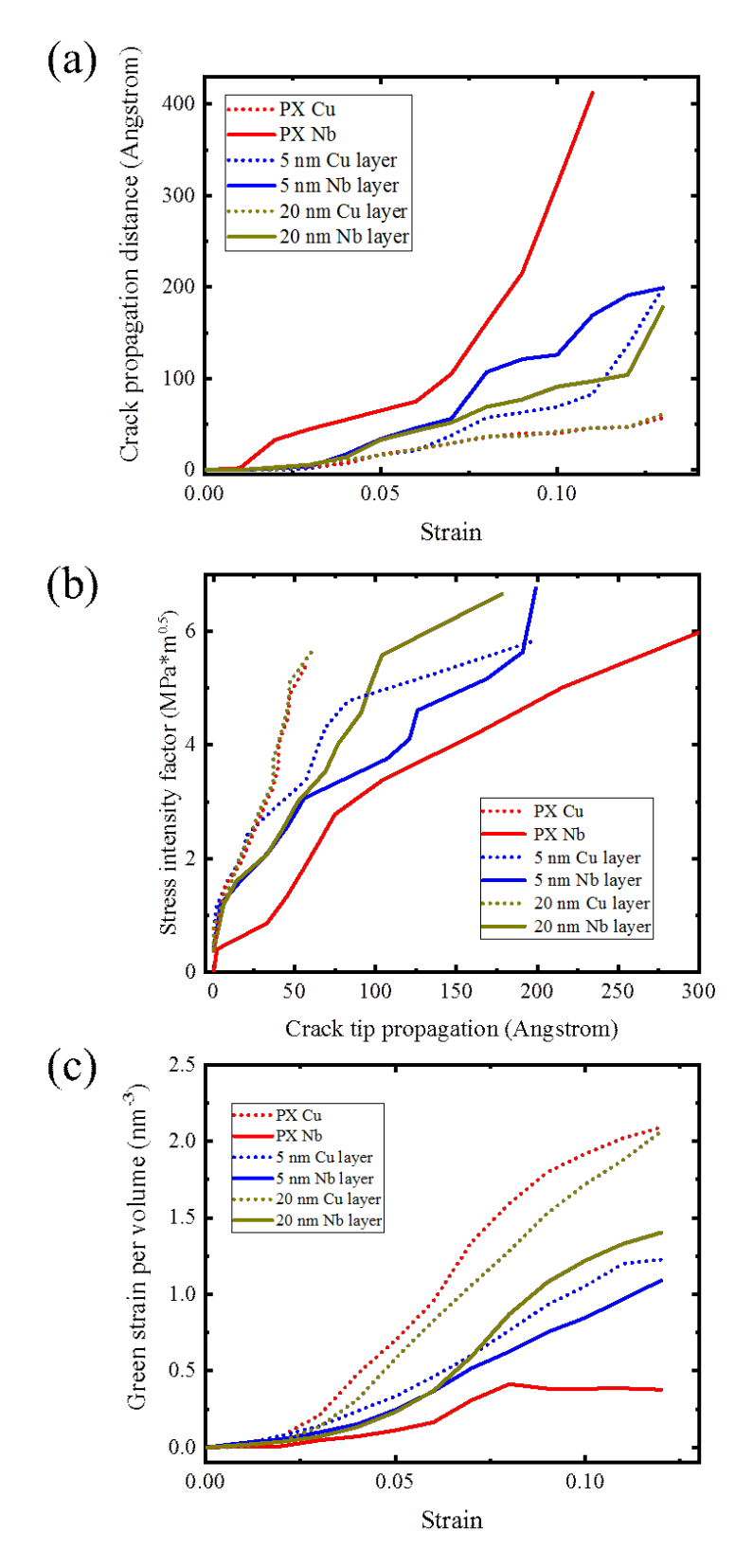


Figure 6. (a) Plot of crack propagation distance for different PX samples. (b) Stress intensity factor for different PX samples. (c) Green strain per volume for different PX samples.